Hiba A. Ajeel
Majid R. Al-Bahrani

Nanomaterials Laboratory, Department of Physics, College of Science, University of Thi-Qar, Thi-Qar,64001, Iraq

Enhancement of Electric Efficiency and Structural Phase Change of $CsPbBr_3$ Caused by Ni^{2+} Doping

This study deals with inorganic perovskite solar cells. Which employs Ni^{2+}-$CsPbBr_3$ as a photon-absorbing layer. In this work, the perovskite layer (Ni^{+2}-$CsPbBr_3$) was prepared using a simple chemical method. The Ni^{+2}-$CsPbBr_3$ samples show spherical and semispherical clusters of particles with homogeneous distribution of nickel nanoparticles on the surface of $CsPbBr_3$. The crystallite size was estimated by using the Scherrer equation. It is shown that Ni doping causes the phase transition of $CsPbBr_3$ from orthorhombic to cubic and also helps to maximize the $CsPbBr_3$ perovskite's crystallinity, which inhibits nonradiative recombination. The Ni^{+2}-$CsPbBr_3$ nanocomposite is a readily produced material, making it suitable for the production of affordable optoelectronic devices.

Keywords: Solar cells; Nickel dopants; Perovskite structures; Spin-coating
Received: 16 April 2024; Revised: 23 June 2024; Accepted: 20 June 2024

1. Introduction

The outstanding optical characteristics of perovskite nanocrystals (NCs) have garnered significant attention, indicating their considerable potential for optoelectronic device design, such as lasers [1-3], photodetectors[4,5], solar cells [6,7], LEDs [8-11], and other optoelectronic devices [12,13]. Pb^{2+} plays a crucial role in the valence and conduction bands, luminescence performance, and structural stability of $CsPbX_3$, which is largely responsible for its exceptional attributes and performance [14,15]. In order to improve stability and optical qualities without altering the features of the host $CsPbX_3$, divalent metal ion doping is typically a helpful technique to partially substitute lead ions [16]. The Ni^{+2} dopant is shown to have a high propensity for octahedral coordination with Br^-, which causes the orthorhombic phase transition to cubic phase and the creation of the $Cs(NiPb)Br_3$ alloy [17,18]. Vincent Joseph Garcias' group study charge transfer and increased light absorption by electrochemically depositing highly-crystalline ZnO nanorods as a scaffold for spin-coated TiO_2 nanoparticles [19]. Shymaa's team used $CsPbBr_3@SiO_2$ quantum dots (QDs) and $CsPbBr_3$ QDs thin films deposited on FTO glass. There were differences in the structural and optical properties between $CsPbBr_3@SiO_2$ quantum dots (QDs) and $CsPbBr_3$ QDs [20]. Kim's group studied altering the Ni doping concentration in $CsPbBr_3$ perovskite. A blue shift is detected in the photoluminescence (PL) spectra with the gradual addition of Ni doping. Compared to undoped PNCs, Ni-doped PNCs have longer lifetimes, stronger light emission, and higher quantum efficiency [21,22]. Thawarkar's team synthesized a nanocube of Ni doped $CsPbBr_3$ nanocrystals (NCs), revealing cubic-rectangular morphologies with varying sizes [23,24]. Chen's team devised a technique to boost the optical efficiency of halide perovskite powder by introducing transition metal Ni ions as dopants. This led to the creation of a $Cs(NiPb)Br_3$ alloy, improved crystallinity, and heightened photoluminescence [25]. Abdulsada's team utilized $PCBM/TiO_3$ as the electron transport material (ETM) and Cu_2O/spiro-OMeTAD/P_3hT/PEDOT:PSS as the hole transport material (HTM) in conjunction with ($CH_3NH_3PbX_3$) (X=I,Cl,Br) as the absorber layer. This is a low p-type-doped, $CH_3NH_3PbX_3$ solid-state planar heterojunction p-i-n solar cell. The n-type and p-type are sandwiched between what is known as the HTM layer. At 263.15K, efficiency was about 22.46% [26]. Abdulsada's team used PCBM as ETM and P_3HT as HTM, where used with the perovskite ($CH_3NH_3PbI_3$) and changed the thickness of ETM from 100 to 2600nm. With this variable, an efficiency of 9.74% was obtained at 263.15K [27]. Our work discovers the phase transition of Ni^{+2}-ion-doped $CsPbBr_3$ and offers a simple approach for producing the Ni^{+2}-$CsPbBr_3$ composite with high optical and electric efficiency.

2. Experiments

Chemicals used in this work were cesium bromide (CsBr, Sigma-Aldrich, 99%), nickel(II) bromide ($NiBr_2$, Sigma-Aldrich, 99.995%), lead bromide ($PbBr_2$, Sigma-Aldrich, 98%) ethanol (C_2H_5OH, Sigma-Aldrich, 99%), N-dimethylformamide (DMF, Sigma-Aldrich, 99.5%). All chemicals were used without further purification unless otherwise noted.

For a typical synthesis, in a three-neck flask, a solution of 1 mmol dried $NiBr_2$, 1 mmol $PbBr_2$ in 30 ml DMF was stirred at 70°C for 2 hours. and the precursor solution was obtained: $NiBr_2/PbBr_2$. Then, adding 1 mmol of CsBr to the previous solution, it was stirred at 70°C for 2 hours. The solution transformed from a yellow green suspension to a transparent one after dissolving. On the FTO glass substrates, the perovskite layer was deposited on

 © ALL RIGHTS RESERVED

FTO/ZnO by the one-step coating method for 10 min. at a speed of 2000 rpm. After being dried in an oven at 150°C to obtain Ni^{+2}-doped $CsPbBr_3$ films, as shown in Fig. (1).

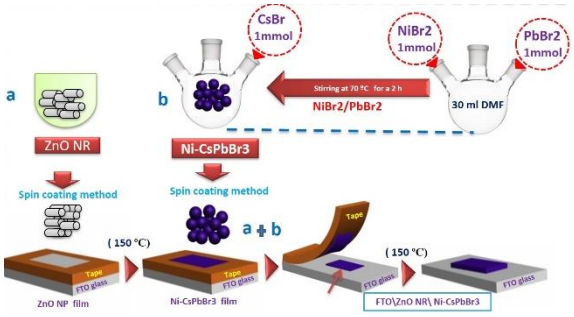

Fig. (1) Schematic diagram of Ni-$CsPbBr_3$ preparation by spin coating method

3. Results and Discussion

The scanning electron microscopy (SEM) image in Fig. (2a) shows the morphology and arrangement of the crystalline rods. Theis SEM image revealed that the flower consisted of numerous distinct nanorods composed of lead bromide ($PbBr_2$). As the crystals elongate in a specific direction, they form microcrystalline rods with varying lengths and widths. Figure (2b) depicts nanosheets of the $CsBr_2$ and the progression details of the crystalline phases present on the surface and their distribution.

In Fig. (3a), the SEM image reveals that the nickel particles have a spherical shape, or are very close to being spherical, and are distributed in a non-uniform manner.The SEM images of Ni^{+2}-$CsPbBr_3$ films. It is easy to find that the original film is made up of many microcrystals that overlap with each other. We also note small nickel particulates that are randomly and widely distributed along the entire surface of the large microstructures this combination provides many benefits and applications for improving optical properties as shown in Fig. (3b). Transmission electron microscopy (TEM) was used to examine structure and internal composition of materials with high accuracy. It is possible to see the lattice flaws, crystal distortions, and crystal structure of the $CsPbBr_3$ thin film (see figures 4a and 4b).

In Fig. (5a), it can be seen that the x-ray diffraction (XRD) pattern of doped $CsPbBr_3$ presents its characteristic diffraction peaks at 22.6°, 31.88°, and 44.9°, corresponding to crystal planes of (110), (200), and (220), respectively, of cubic phase $CsPbBr_3$ (PDF vo. 75-0412). It is noteworthy that adding Ni^{+2} to the $CsPbBr_3$ crystal causes an orthorhombic to cubic phase change. Smaller doping cations are generally thought to be responsible for the contraction of the perovskite in the $CsPbBr_3$ NC lattice because Ni^{+2} doping can effectively remove intrinsic defects like halide vacancies and enhance both the lattice's short range and local structural order [28].

(a)

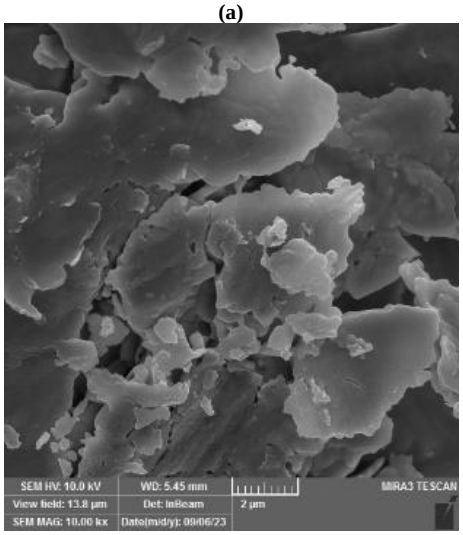

(b)

Fig. (2) SEM images of (a) $PbBr_2$, and (b) CsBr

The evolution of the crystalline structure of the $PbBr_2$ samples was further studied using XRD (Fig. 5b). A reasonably broad peak is seen within 21.5°-37.7° in the XRD pattern. Also we observed some weak diffraction peaks. The experimental peaks closely match the standard (JCPDS card no. 00-030-0697) [29]. In Fig. (5c), the diffraction from the (110) plane at 29.5° was quite intense. Its appearance indicated that it was a perfectly crystalline, defect-free cubic phase. The experimental peaks of CsBr closely match the standard (JCDP card no. 01-073-0391) [30]. In Fig. (5d), the characteristic lattice parameters of Ni component are a=b=c=3.524Å according to JCPDS card no. 04-0850, which showed that Ni has a face-centered cubic (FCC) phase structure. Furthermore, the Ni peaks located at 2θ=44.51° (d=2.034Å), 51.85° (d=1.762Å) and 76.37° (d=1.246Å) were related to (111), (200), and (220) planes, respectively [31].

 © ALL RIGHTS RESERVED

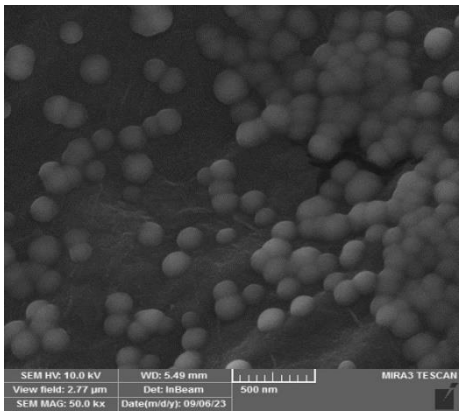

(a)

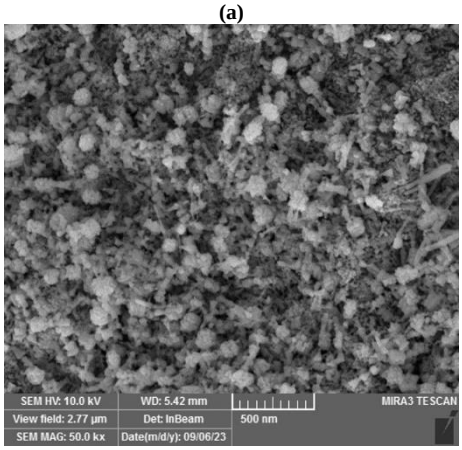

(b)

Fig. (3) SEM images of (a) Ni ,(b)Ni^{+2}-$CsPbBr_3$

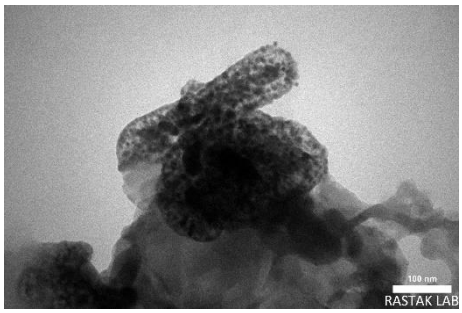

(a)

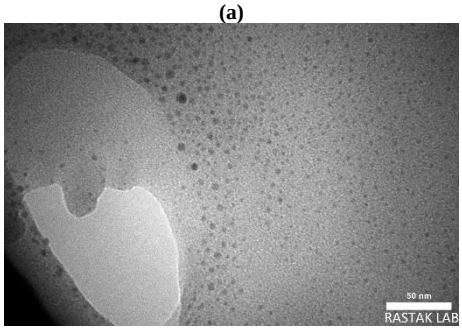

(b)

Fig. (4) TEM images of Ni^{+2}-$CsPbBr_3$

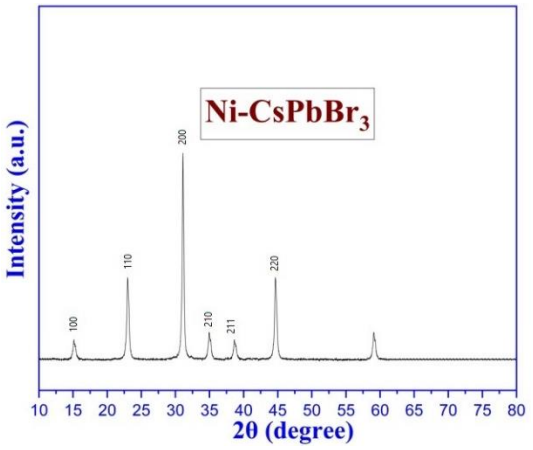

(a)

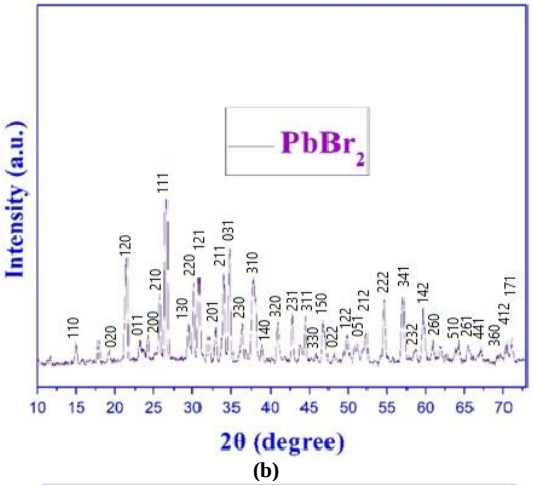

(b)

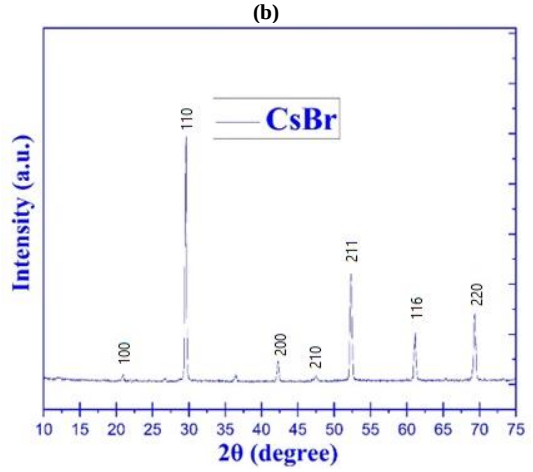

(c)

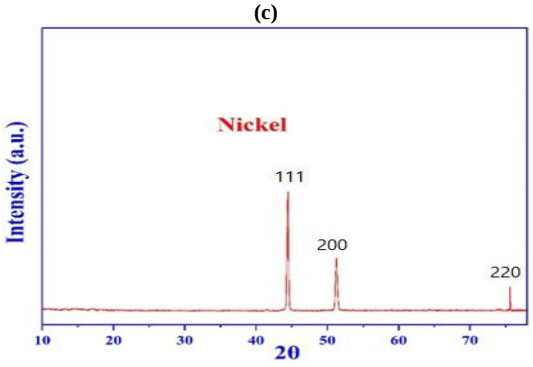

(d)

Fig. (5) XRD patterns of (a) Ni^{2+}- $CsPbBr_3$, (b) $PbBr_2$, (c) CsBr, and (d) Ni^{2+}

 © ALL RIGHTS RESERVED

The fitting parameters, mainly the open-circuit voltage (V_{OC}), short-circuit current (I_{SC}), and fill factor (F.F), were determined from the I-V characteristics of the solar cells in table (1) for the $CsPbBr_3$ samples. Increasing Ni^{2+} doping concentration from 10% to 30% lead to increase the power conversion efficiency (PCE) correspondingly from 9.8568% to 11.8932%. In this process, the radiative recombination behavior is well encouraged while the nonradiative recombination is restrained. With further increasing the doping concentration, PCE slightly decreases. Therefore, there is an optimal amount of Ni^{2+} doping in $CsPbBr_3$ to inspire the enhancement in PCE rather than increasing the defect related recombination rate as in Fig. (6).

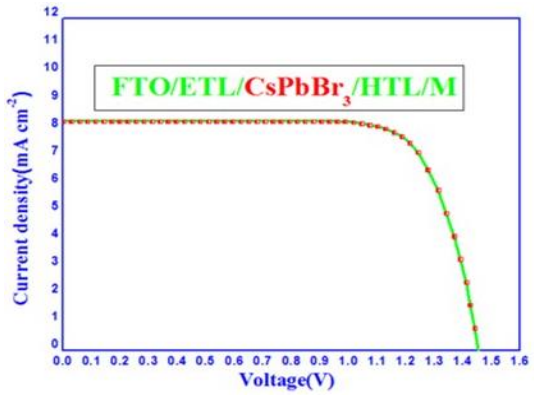

(a)

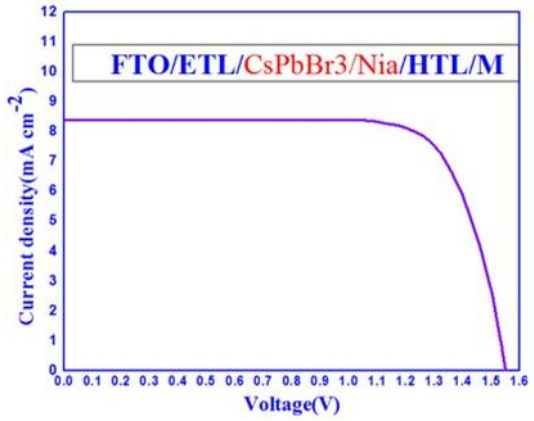

(b)

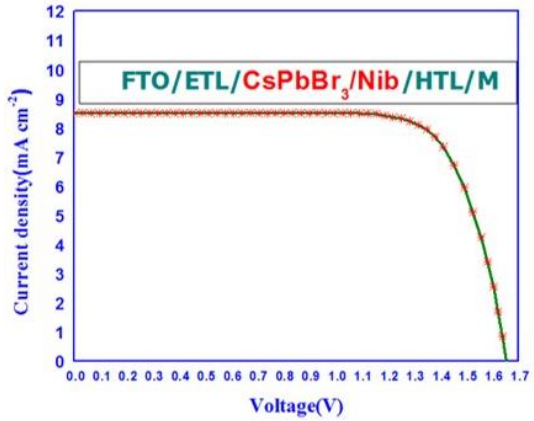

(c)

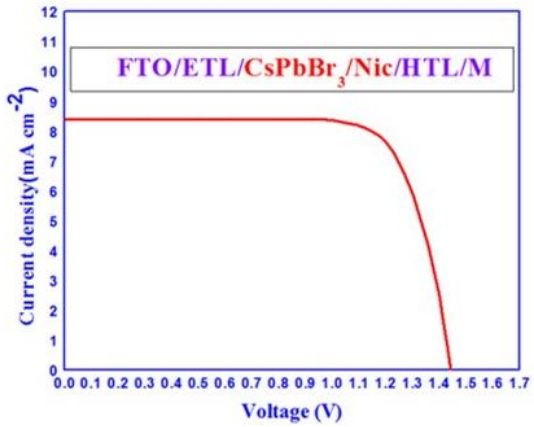

(d)

Fig. (6) Performance of all perovskite solar cells

The PCE of a solar cell is the percentage ratio of the solar cell's maximum power output (P_{max}) to the power of the incident light (P_{in}), as shown in the following equation:

$$PCE = FF \times \frac{Jsc \times Voc}{P_{in}} \times 100 \qquad (1)$$

where J_{max} is the current density at the maximum power output in the J-V curves

Figure (7) shows the absorption spectra as function of the Ni doping concentration using a UV-Visible spectrophotometer in the wavelength range 200-1200nm. The first exciton peaks of Nib-$CsPbBr_3$ shifted to higher energies with increasing Ni^{2+} concentration 20%. At wavelength of 500nm, $CsPbBr_3$ had an absorbance of 0.75, and the absorbance for $CsPbBr_3$-Nib films in the wavelength range of 400-500nm increased from 0.8 to 0.95. Additionally, we observe that the addition of nickel nanoparticles causes the perovskite $CsPbBr_3$ to absorb more light because these particles help the material's optical absorption range to expand into wider spectral regions. This can increase the amount of light absorbed, which in turn increases the absorption of ligh.

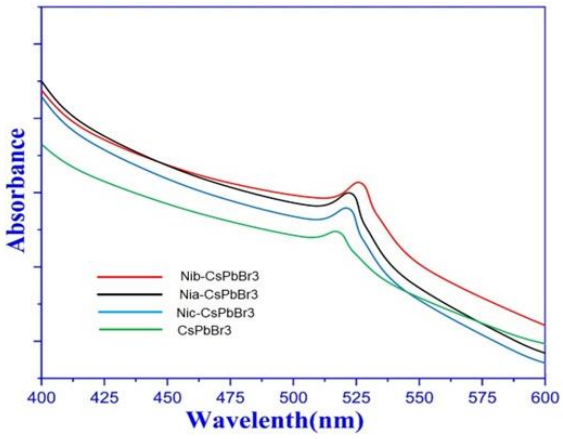

Fig. (7) The absorption spectra of $CsPbBr_3$, $CsPbBr_3$-Nia, $CsPbBr_3$-Nib, and $CsPbBr_3$-Nic

 © ALL RIGHTS RESERVED

Table (1) Photovoltaic parameters of PSCs for all configurations

Solar cells (Configurations)	Jsc (mA/cm^2)	Voc (V)	F. F	PCE (%)
FTO/ETL/$CsPbBr_3$/HTL/M	8.29	1.45	0.82	9.8568
FTO/ETL/$CsPbBr_3$-Nia/HTL/M	8.40	1.57	0.84	11.0779
FTO/ETL/$CsPbBr_3$-Nib/HTL/M	8.48	1.65	0.85	11.8932
FTO/ETL/$CsPbBr_3$-Nic/HTL/M	8.37	1.49	0.82	10.2264

4. Conclusion

We have successfully synthesized the Ni-$CsPbBr_3$ nanocomposite by a simple chemical method. The structural phase transition of $CsPbBr_3$ from an orthorhombic phase to a cubic one can be induced by the lattice contraction after incorporating the Ni ions. The value of the PCE reaches a maximum of 11.8932% at an optimal Ni doping of 20%. The photoluminescence efficiency increases and the nonradiative combination is positively restricted by the Ni^{2+} doping. Our research offers a simple method for producing the Ni-$CsPbBr_3$ composite, which is less hazardous at low temperatures and in an ambient setting. This material can be a competitive contender for applications involving color conversion and light emission.

References

[1] F. Deschler et al., "High photoluminescence efficiency and optically pumped lasing in solution-processed mixed halide perovskite semiconductors", *J. Phys. Chem. Lett.*, 5(8) (2014) 1421-1426.

[2] J. Xing et al., "Vapor phase synthesis of organometal halide perovskite nanowires for tunable room-temperature nanolasers", *Nano Lett.*, 15(7) (2015) 4571-4577.

[3] H. Zhu et al., "Lead halide perovskite nanowire lasers with low lasing thresholds and high quality factors", *Nat. Mater.*, 14(6) (2015) 636–642.

[4] J. Xue et al., "Narrowband perovskite photodetector-based image array for potential application in artificial vision", *Nano Lett.*, 18(12) (2018) 7628–7634.

[5] J. Song et al., "Monolayer and Few-Layer All-Inorganic Perovskites as a New Family of Two-Dimensional Semiconductors for Printable Optoelectronic Devices", *Adv. Mater.*, 28(24) (2016) 4861–4869.

[6] P. Luo et al., "Solvent engineering for ambient-air-processed, phase-stable $CsPbI_3$ in perovskite solar cells", *J. Phys. Chem. Lett.*, 7(18) (2016) 3603–3608.

[7] L.-J. Chen et al., "Synthesis and optical properties of lead-free cesium tin halide perovskite quantum rods with high-performance solar cell application", *J. Phys. Chem. Lett.*, 7(24) (2016) 5028–5035.

[8] M. Ban et al., "Solution-processed perovskite light emitting diodes with efficiency exceeding 15% through additive-controlled nanostructure tailoring", *Nat. Commun.*, 9(1) (2018) 3892.

[9] J. Li et al., "50-Fold EQE improvement up to 6.27% of solution-processed all-inorganic perovskite $CsPbBr_3$ QLEDs via surface ligand density control", *Adv. Mater.*, 29(5) (2017) 1603885.

[10] J. Song et al., "Quantum Dot Light-Emitting Diodes Based on Inorganic Perovskite Cesium Lead Halides ($CsPbX_3$)", *Adv. Mater.*, 27(44) (2015) 7162–7167.

[11] J. Song et al., "Room-temperature triple-ligand surface engineering synergistically boosts ink stability, recombination dynamics, and charge injection toward EQE-11.6% perovskite QLEDs", *Adv. Mater.*, 30(30) (2018) 1800764.

[12] J. Wang et al., "Spin-optoelectronic devices based on hybrid organic-inorganic trihalide perovskites", *Nat. Commun.*, 10(1) (2019) 129.

[13] M. Kepenekian et al., "Rashba and Dresselhaus effects in hybrid organic–inorganic perovskites: from basics to devices", *ACS Nano*, 9(12) (2015) 11557–11567.

[14] Q.A. Akkerman et al., "Genesis, challenges and opportunities for colloidal lead halide perovskite nanocrystals", *Nat. Mater.*, 17(5) (2018) 394–405.

[15] J.M. Yaseen, "Crystal Structures and Curie's Temperature of ABO_3 Perovskite Ceramics with Different Ionic Radius", *Iraqi J. Mater.*, 1(2) (2022) 75-82.

[16] J. Navas et al., "New insights into organic–inorganic hybrid perovskite CH_3 NH_3 PbI_3 nanoparticles. An experimental and theoretical study of doping in Pb^{2+} sites with Sn^{2+}, Sr^{2+}, Cd^{2+} and Ca^{2+}", *Nanoscale*, 7(14) (2015) 6216–6229.

[17] T. Lei et al., "Electrical and optical tunability in all-inorganic halide perovskite alloy nanowires", *Nano Lett.*, 18(6) (2018) 3538–3542.

[18] G. Kim et al., "Impact of strain relaxation on performance of α-formamidinium lead iodide perovskite solar cells", *Science (80-)*, 370(6512) (2020) 108–112.

[19] V.J. Garcia, C.M. Pelicano and H. Yanagi, "'Low temperature-processed ZnO nanorods-TiO_2 nanoparticles composite as electron transporting layer for perovskite solar cells", *Thin Solid Films*, 662 (2018) 70–75.

[20] S.K. Hussian and M.R. Al-bahrani, "Influence of SiO_2 nanoparticles on the structural, morphology , and optical properties of $CsPbBr_3$ Quantum Dots", *J. Polym. Compos.*, 11(2) (2023) 62–69.

[21] H. Kim *et al.*, "Enhanced optical properties and stability of $CsPbBr_3$ nanocrystals through nickel doping", *Adv. Funct. Mater.*, 31(28) (2021) 2102770.

 © ALL RIGHTS RESERVED

[22] Yasir A. Baydhon, "Pulsed-Laser Deposition of Nanostructured Nickel Oxide-Doped Tellurium Oxide Thin Films", *Iraqi J. Mater.*, 1(3) (2022) 139-144.
[23] S. Thawarkar et al., "Ni-doped $CsPbBr_3$ perovskite: synthesis of highly stable nanocubes", *Langmuir*, 35(52) (2019) 17150–17155.
[24] F.A. Ahmed and A.H. Majeed, "Characteristics of NiO-Doped TeOThin FilmsPrepared by Pulsed-Laser Deposition", *Iraqi J. Mater.*, 2(2) (2023) 89-96.
[25] T. Chen et al., "Ni^{2+} doping induced structural phase transition and photoluminescence enhancement of $CsPbBr_3$", *AIP Adv.*, 11(11) (2021).
[26] Z.R. Abdulsada et al., "High Efficiency (22.46) of Solar Cells Based on Perovskites", *Univ. Thi-Qar J. Sci.*, 10(2) (2023) 187–191.
[27] Z.R. Abdulsada and S.M. AbdulAlmohsin, "High Efficiency Solar Cells Base on Organic-inorganic Perovskites Materials", *Univ. Thi-Qar J. Sci.*, 8(2) (2021) 23–29.
[28] Z.-J. Yong et al., "Doping-enhanced short-range order of perovskite nanocrystals for near-unity violet luminescence quantum yield", *J. Am. Chem. Soc.*, 140(31) (2018) 9942–9951.
[29] Y. Hu et al., "$CsPbBr_3@SiO_2$ Core–Shell Nanoparticle Films for Superhydrophobic Coatings", *ACS Appl. Nano Mater.*, 4(6) (2021) 6306–6315.
[30] V. Santhana et al., "Synthesis and emission characteristics of lead-free novel Cs_4SnBr_6/SiO_2 nanocomposite", *Mater. Lett.*, 280 (2020) 128562.
[31] S. Bi et al., "Enhanced electromagnetic interference shielding effects of cobalt-nickel polyalloy coated fabrics with assistance of rare earth elements", *Fibers Polym.*, 19 (2018) 1084–1093.

 © ALL RIGHTS RESERVED